Celestial Mechanics and Dynamical Astronomy (2005) 92:157–188
DOI 10.1007/s10569-004-0029-0 

# GLOBAL DYNAMICS IN SELF-CONSISTENT MODELS OF ELLIPTICAL GALAXIES

C. KALAPOTHARAKOS[1,2] and N. VOGLIS[1]
[1]*Academy of Athens, Research Center for Astronomy, 4 Soranou Efesiou, GR-11527, Athens, Greece, e-mail: ckalapot@cc.uoa.gr; nvogl@cc.uoa.gr*
[2]*Department of Physics, Section of Astrophysics, University of Athens, Panepistimiopoli, Athens GR 15783, Greece*

(Received: 7 September 2004; revised: 9 December 2004; accepted: 31 December 2004)

**Abstract.** We compare two different N-body models simulating elliptical galaxies. Namely, the first model is a non-rotating triaxial N-body equilibrium model with smooth center, called SC model. The second model, called CM model, is derived from the SC by inserting a central mass in it, so that all possible differences between the two models are due to the effect of the central mass. The central mass is assumed to be mainly due to a massive central black hole of mass about 1% of the total mass of the galaxy. By using the fundamental frequency analysis, the two systems are thoroughly investigated as regards the types of orbits described either by test particles, or by the real particles of the systems at all the energy levels. A comparison between the orbits of test particles and the orbits of real particles at various energy levels is made on the rotation number plane. We find that extensive stable regions of phase space, detected by test particles remain empty, i.e. these regions are not occupied by real particles, while many real particles move in unstable regions of phase space describing chaotic orbits. We run self-consistently the two models for more than a Hubble time. During this run, in spite of the noise due to small variations of the potential, the SC model maintains (within a small uncertainly) the number of particles moving on orbits of each particular type. In contrast, the CM model is unstable, due to the large amount of mass in chaotic motion caused by the central mass. This system undergoes a secular evolution towards an equilibrium state. During this evolution it is gradually self-organized by converting chaotic orbits to ordered orbits mainly of the short axis tube type approaching an oblate spheroidal equilibrium. This is clearly demonstrated in terms of the fundamental frequencies of the orbits on the rotation number plane and the time evolution of the triaxiality index.

**Key words:** chaos, frequency maps, N-body simulations, galaxies: elliptical, galaxies: evolution

## 1. Introduction

Self-consistent galactic models realized by N-body simulations are efficient tools in studying the structure and evolution of galaxies. We use these tools in investigating the orbital structure, the evolution and the stability of models simulating elliptical galaxies.

If we assume that elliptical galaxies are non-rotating triaxial equilibrium configurations with a smooth center, i.e. the density near the center is flat, the potential in this region tends to be harmonic. The most favored type of ordered orbits in this case is the type of box orbits, i.e. orbits composed of three oscillations along the corresponding principal axes of the anisotropic system. They satisfy three integrals of motion, which are approximately the energies along the three axes of the box. The pericenters of these orbits can be arbitrarily close to the center.

In real galaxies, in principle, the central region may not be smooth. In many cases the density near the center, instead of being flat, presents a cuspy density profile (Ferrarese et al., 1994; Lauer et al., 1995; Gebhardt et al., 1996; Faber et al., 1997). Furthermore, the dominant opinion today is that the center is occupied by a black hole. Recent investigations provide accumulated evidence that massive central black holes in galaxies must be quite common (Kormendy and Richstone, 1995; Kormendy et al., 1997, 1998; van der Marel et al., 1997, 1998; Magorrian et al., 1998; Cretton and van den Bosch 1999; Gebhardt et al., 2000). The massive central black holes may be surrounded by other types of mass, e.g. gas, clouds, stars, etc.

The dynamical effect of a central force field (produced by a massive central black hole and its direct environment) on the orbits of stars in a galaxy is important. Orbits passing near the center are appreciably deflected by the central force field that dominates locally. As a consequence, the integrals of motion of ordered orbits are destroyed when these orbits approach the center. Thus, the orbits become chaotic (Gerhard and Binney 1985; Merritt and Fridman 1996).

This effect may have important consequences on the stability of galaxies. This field of research is very active in recent years (e.g. Merritt and Fridman, 1996; Merritt and Valluri, 1996; Fridman and Merritt, 1997; Valluri and Merritt, 1988; Merritt and Quinlan, 1998; Siopis, 1999; Siopis and Kandrup, 2000; Kandrup and Sideris, 2002; Poon and Merritt, 2002, 2004; Kandrup and Siopis, 2003; Kalapotharakos et al 2004; Voglis and Kalapotharakos, 2005)

In order to investigate further this problem, we concentrate our study on a comparison between the following two models:

(i) a triaxial N-body model with smooth center in virial equilibrium, hereafter called Smooth Center (SC) model and
(ii) a model, called Central Mass (CM) model, that is created from the SC model by inserting a central mass. The central mass is assumed to be mainly due to a black hole of size comparable to the largest masses of black holes in the centers of galaxies estimated from observational data.

The comparison regards the various types of orbits described by the individual particles in each system, as they are mapped on the space of their fundamental frequencies. It is obvious that all the differences between the two models must be attributed to the presence of the central mass.

As we will see below, this comparison reveals important features of the dynamical role a central black hole can play in real galaxies, such as the destabilization of orbits of certain types (e.g. box orbits) or enhancement of the stability of other types (e.g. short axis tube orbits). We show that redistribution of different types of orbits can take place, so that the system develops a secular evolution towards a new equilibrium configuration.

In Section 2 we describe the main features of the two models (Sections 2.1 and 2.2, respectively). In Section 3 we give a short description of the method developed earlier (Voglis et al., 2002) to distinguish the mass in chaotic motion from the mass in ordered motion in N-body models and explain how this method is applied in our problem. We use also the frequency analysis method to make a similar distinction and we compare the results of the two methods. In Section 4, we use the frequency analysis method to identify all the types of orbits of test particles in the SC model and compare them with the orbits of the real particles of the system on the rotation number plane i.e. the plane of the two fundamental frequencies of oscillation of the orbits along the middle and the longest axis, respectively, divided by the fundamental frequency along the shortest axis. The types of orbits that appear at various energy levels are examined. In Section 5 the same method is applied at a particular snapshot of the CM model to identify the various types of orbits on the rotation number plane and compare with the results of Section 4. In section 6 the secular evolution of the CM model is examined by representing the orbits on the rotation number plane at different snapshots of the system. Our conclusions are summarized in Section 7.

## 2. Description of the Models

### 2.1. THE SC MODEL

The derivation of the smooth center model is described in detail in previous papers (Contopoulos et al., 2002; Voglis et al., 2002). In brief, this N-body model is the outcome of dissipationless collapse and relaxation derived from quiet cosmological initial conditions. In the relaxed equilibrium configuration this model is characterized by a triaxial bar. Let the principal axes, shortest, intermediate and longest axes be respectively along the $x,y,z$ cartesian axes. The maximum ellipticity of the equidensity contours (on the $x$–$z$ plane) in the inner

parts is of E7 type, while it tends to an E5 type in the outer parts (on the same plane).

The number of particles used is $N \simeq 1.5 \times 10^5$. The evolution is followed by a N-body code based on the conservative technique Allen et al., 1990 In this code the Poisson equation is solved in terms of an orthogonal set of basis functions (Spherical Bessel functions and Spherical Harmonics). The potential provided by this technique is smooth. Particles do not see their neighbors. They move under the global field created by their distribution at any time. In the central region this potential is roughly harmonic. In its typical version the code gives the global potential expanded in 120 terms. In spherical coordinates $(r, \theta, \phi)$ the radial expansion is extended up to 20 terms and the angular expansions $(\theta, \phi)$ up to quadrupole terms. Among the 120 terms, 20 are monopole terms (depending only on $r$), 20 quadrupole terms (depending on $r$ and $\theta$) and 80 triaxial terms (depending on the three coordinates). This potential can be written as

$$
\begin{aligned}
V(r,\theta,\phi) = & \underbrace{\sum_{l=0}^{19} B_{l00} V_{l00}(r)}_{\text{20 monopole terms}} + \underbrace{\sum_{l=0}^{19} B_{l20} V_{l20}(r,\theta)}_{\text{20 quadrupole terms}} \\
& + \sum_{l=0}^{19} B_{l21} V_{l21}(r,\theta) \cos\phi + \sum_{l=0}^{19} C_{l21} V_{l21}(r,\theta) \sin\phi \\
& \underbrace{+ \sum_{l=0}^{19} B_{l22} V_{l20}(r,\theta) \cos 2\phi + \sum_{l=0}^{19} C_{l22} V_{l20}(r,\theta) \sin 2\phi}_{\text{80 triaxial terms}}
\end{aligned}
\tag{1}
$$

where $B_{l00}, B_{l20}, B_{l21}, C_{l21}, B_{l22}, C_{l22}$ (with $l = 0, \ldots, 19$) are the coefficients of the expansion.

The adopted scaling units are as follows. The unit of energy is defined so that the value of the potential at the center (deepest value) of the SC model is equal to $V(0) = -100$. The length unit is the half mass radius $R_h$ of this system. The time unit is the half mass crossing time defined as $T_{\rm hmct} = (2R_h^3/GM_g)^{1/2}$ in terms of $R_{\rm h}$ and the mass $M_{\rm g}$ of the galaxy.

It is useful to express some important time scales in this unit. The period $T_{\rm cp}$ of a circular orbit of radius $R_h$ is $T_{\rm cp} = 2\pi T_{\rm hmct}$. The relation between the radial period $T_{\rm r}$ of an orbit (i.e. the time needed for a star to go from the pericenter to the apocenter and back to the pericenter of its orbit) and the circular period $T_{\rm cp}$ of the same energy can be written as $T_{\rm cp} = fT_{\rm r}$ where the factor $f$ is $f = 1$ in the Kelperian potential, and $f = 2$ in the harmonic

potential. In the potential of our N-body system $f$ ranges between these two values. For orbits of the N-body systems with energies near the value of the potential at the half mass radius, the values of $f$ are close to 2.

The radial period of the orbits with energy equal to the mean value of the potential at the half mass radius, denoted by $T_{\rm hmr}$, is $T_{\rm hmr} \approx 3T_{\rm hmct}$. A star in circular motion, in a typical galaxy, describes about 50 cycles in a Hubble time $t_{\rm Hub}$. Therefore, a Hubble time can be written as

$$t_{\rm Hub} \approx 50T_{\rm cp} = 50fT_{\rm hmr} \approx 300T_{\rm hmct}. \tag{2}$$

In a self-consistent run the coefficients of the potential (1) are re-evaluated at regular small time steps $\Delta t = 0.025T_{\rm hmct}$. The variations of the coefficients in this model are quite small. They have only a small noise depending on the number N of particles, i.e. of the order of $1/\sqrt{N} \lesssim 1\%$.

If the coefficients of the potential are fixed at a given snapshot we can write an autonomous 3D Hamiltonian

$$H = \frac{\dot{r}^2}{2} + \frac{L_\phi^2}{2r^2 \sin\,\theta^2} + \frac{L_\theta^2}{2r^2} + V(r, \theta, \phi). \tag{3}$$

Using this Hamiltonian we can study the phase space of the system. We can find the various types of orbits using test particles and compare with the orbits of the real particles of the system in this Hamiltonian.

Any possible changes in the types of orbits, due to the variations of the coefficients in time, can be checked if we fix the values of the coefficients at a different snapshot and repeat the study of the Hamiltonian (3). No serious changes are detected in the phase space of this model even after run times that considerably exceed the Hubble time.

### 2.2. THE CM MODEL

We choose a particular snapshot of the SC model (after a run time of $t_{\rm SC} = 100T_{\rm hmct}$ in the relaxed configuration). At this snapshot the time is reset to $t = 0$ and a central mass of a given size is inserted abruptly to create the CM model. So all the differences between the two models can be attributed to the presence of the central mass of this size.

We consider the case when the time of growth of the central black hole is much less than the galaxy's life time. In this case the main dynamical effect of the black hole depends mainly on its final size. For this reason we simplify the model by neglecting the transient period of growth of the black hole and we insert abruptly the central mass.

For the central mass $M_{\rm cm}$, we have adopted the central potential

$$V_{\rm cm}(r) = \frac{GM_{\rm cm}}{a}\left[\arctan\left(\frac{r}{a}\right) - \frac{\pi}{2}\right], \tag{4}$$

where $a$ is a softening length given by

$$a = 0.05 \frac{M_{\rm cm}}{M_{\rm g}} R_{\rm g}, \tag{5}$$

where $R_g$ is the radius of the galaxy. Notice that the force derived from this potential is

$$F_{\rm cm}(r) = -\frac{\rm G\ M_{cm}}{r^2 + a^2}, \tag{6}$$

i.e. it is of a Keplerian nature only for orbits with pericenters much larger than $a$. The force at the center of this model tends to a finite constant. Stars with pericenters below the softening length $a$ are not deflected strongly by the CM. This softening length does not significantly alter the global behavior of the system, since the number of orbits with pericenters less than $a$ is small.

Notice that the density profile derived from the above potential is

$$\rho_{\rm cm}(r) = \frac{\rm G\ M_{cm} a^2}{2\pi r (r^2 + a^2)^2}, \tag{7}$$

i.e. this model for $r < a$ gives an $r^{-1}$ cuspy density profile.

The relative size $m$ of the central mass with respect to the mass of the galaxy, i.e.

$$m = M_{\rm cm}/M_{\rm g} \tag{8}$$

is an important parameter. In the CM model we use the value of $m = 0.01$. Such a value is of the same order of magnitude as the largest black hole masses estimated by observational data (Magorrian et al., 1998; Merritt and Ferrarese, 2001).

In this model, particles move under the superposition of the potential (4) and the potential due to their distribution in space at any time given by (1) in which the coefficients are re-evaluated at every small time step ($\Delta t = 0.025 T_{\rm hmct}$).

Notice that after the introduction of the central mass the radial profile of the density of particles near the center does not remain so flat as before. It develops a weekly cuspy profile.

In order to study the types of orbits which are consistent with a given snapshot of the total potential we fix the coefficients in (1) at this particular snapshot and we run the particles in the autonomous Hamiltonian

$$H = \frac{\dot{r}^2}{2} + \frac{L_\phi^2}{2r^2 \sin^2\theta} + \frac{L_\theta^2}{2r^2} + V(r, \theta, \phi) + V_{\rm cm}(r). \tag{9}$$

As we will see in Section 6 this model presents a secular evolution that can be studied by applying (9) at many successive snapshots of the potential.

## 3. Distinction of Particles in Ordered Motion from Particles in Chaotic Motion

As a consequence of the non-integrability of the potential (1) a considerable part of the orbits in the two systems are chaotic.

In Voglis et al. (2002) we have developed a method to identify particles of N-body models moving in chaotic orbits provided that their mean logarithmic divergence rate exceeds a certain threshold.

In brief this method of distinguishing the chaotic from ordered orbits is based on the combination of two different tools. First, is the calculation of the mean exponential divergence in a given period of time, between the orbit of a real particle in the system and a neighboring orbit. The mean exponential divergence is measured in units of the inverse radial period $T_{\rm rj}$ of the particular orbit $j$. We call it Specific Finite Time Lyapunov Characteristic Number (S-FT-LCN) and we use simply the symbol $L_{\rm j}$ for it. The orbit j is integrated in a 3D autonomous Hamiltonian, as the Hamiltonians (3) or (9) when they are applied to a particular snapshot of the potential (1).

Second, we use the Alignment Index $\mathrm{AI_j}$ of the orbit j, i.e. the magnitude of the sum or the difference of two initially arbitrary deviation vectors of this orbit, normalized to unity at every $\Delta t$.

If the orbit is chaotic, the two deviation vectors tend exponentially to be parallel or antiparallel (depending on their initial orientation). In this case, the alignment index $\mathrm{AI_j}$, expressed by the difference of the deviation vectors if they are parallel, or by the sum if they are antiparallel, i.e. the smaller value between the two, tends exponentially to zero (Voglis et al., 1998, 1999; Skokos 2001).

If the orbit is ordered, or if it is so weakly chaotic that the chaotic character can not appear during the available integration time, the two deviation vectors oscillate around each other. Thus, the corresponding values of $\mathrm{AI_j}$ do not tend exponentially to zero, but instead they maintain finite values, in principle close to unity. (It is very improbable to become less than $10^{-3}$).

The run time $t_{\rm j}$ of the orbit j is $t_{\rm j} = N_{\rm rp} T_{\rm rj}$, where $N_{\rm rp}$ is a number of radial periods common for all the orbits. In the case of ordered orbits, or chaotic orbits that temporarily behave as ordered, the values of $L_{\rm j}$ decrease on the average as $N_{\rm rp}^{-1}$ and they are almost independent of the orbit. As $N_{\rm rp}$ increases, the $L_{\rm j}$ of chaotic orbits stops decreasing and it is saturated at a roughly constant value $L_{\rm j} > N_{\rm rp}^{-1}$. Chaotic orbits are characterized by such constant values of $L_{\rm j}$. The detection limit of chaotic orbits is determined by the maximum number of radial periods $N_{\rm rp-max}$. For the adopted value $N_{\rm rp-max} = 1200$ the minimum $L_{\rm j}$ of the detected chaotic orbits is the threshold of $\simeq 10^{-2.8}$.

The index $L_j$ gives the rate of exponential divergence per radial period. The advantage of using $L_j$ is the fact that the values of $L_j$ measure the chaotic character independently of the characteristic time scale of the orbit. If the value of $L_j$ is smaller than the threshold the orbit is either ordered, or close to ordered, obeying two integrals of motion (at least approximately) beyond its binding energy. In this sense the index $L_j$ is a measure of the departure from integrability, or in other words, $L_j$ is a measure of the complexity of the phase space of the orbit.

The Lyapunov time derived from $L_j$, i.e. the time $L_j^{-1}$ is expressed in radial periods $T_{rj}$ and corresponds to different real time scales depending on the size of $T_{rj}$. Such a Lyapunov time, $L_j^{-1}$, cannot be directly compared with a fixed time scale, for example, the Hubble time. Furthermore, the threshold value of this Lyapunov time, derived from the threshold value of $L_j = 10^{-2.8}$, is smaller for orbits of short radial periods (innermost orbits, i.e. orbits of low binding energies) than for orbits of long radial periods.

In Voglis et al. (2002), we have also used the CU-FT-LCN, of simply $L_{cuj}$, i.e., the Finite Time LCN measured in a common time unit for all the orbits, equal to the inverse radial period $T_{hmr}$ of an orbit with energy equal to the mean value of the potential at the half mass radius. The index $L_{cuj}$ gives the total exponential divergence in time $T_{hmr}$, independently of the number of radial periods during this time. This quantity measures the combined action of two effects, i.e the chaotic character of the orbit and the characteristic time scale of the orbit. For the innermost orbits (where $T_{rj} < T_{hmr}$), $L_{cuj}$ takes larger values than the corresponding values of $L_j$, while for the outermost orbits it takes smaller values than $L_j$. If the value of $L_{cuj}$ is smaller than the adopted threshold there is no guarantee that the orbit obeys other integrals of motion beyond its binding energy. Very small values of $L_{cuj}$ can be derived for long period orbits, even if they wander in a large chaotic sea. Therefore, $L_{cuj}$ is not an objective measure of the departure from integrability, because its values are biased by the dynamical time scales of the orbits. For this reason we prefer using $L_j$ instead $L_{cuj}$ for distinguishing the orbits.

However, $L_{cuj}$ is also a useful quantity because the Lyapunov times $L_{cuj}^{-1}$, expressed in common units $T_{hmr}$, can be directly compared to the Hubble time. Furthermore, a particular threshold value of $L_{cuj}$ defines a common threshold value of the Lyapunov times for all the orbits independently of their characteristic time scales.

As a consequence of the above properties of the two indices, the number of chaotic orbits, that can be detected by using a threshold value in $L_{cuj}$, is not exactly the same with those detected by using the same threshold value in $L_j$. The threshold of $L_{cuj}$ gives more chaotic orbits in the inner parts, while the threshold of $L_j$ gives more chaotic orbits in the outer parts. However, provided that the adopted thresholds are small enough, so that the minimum

Lyapunov times considerably exceed the Hubble time, the difference between the two sets of the detected chaotic orbits regards only very weakly chaotic orbits that might equally well be considered as ordered orbits.

Large values of $L_{\rm j}$ are correlated with large variability per radial period of the actions of the orbits and hence with larger rates of chaotic diffusion (Lichtenberg and Lieberman 1992). Chaotic diffusion, however, is important in a given time provided that this time is longer than the Lyapunov time. The values of $L_j$ can give us the ability of chaotic diffusion in a given number of radial periods, but not in a fixed period of time. Thus, after obtaining the separation of chaotic orbits in terms of $L_j$, we find the chaotic orbits that can in principle develop chaotic diffusion in a Hubble time, by calculating their $L_{cuj}$ in terms of their $L_j$ as

$$L_{\rm cuj} = L_{\rm j} \frac{T_{\rm hmr}}{T_{\rm rj}}. \tag{10}$$

As mentioned above, the Lyapunov time $L_{\rm cuj}^{-1}$, expressed in units of $T_{\rm hmr}$, can be directly compared with the Hubble time $t_{\rm Hub} \simeq 100 T_{\rm hmr}$. Therefore, a necessary condition for a remarkable chaotic diffusion in one Hubble time is $L_{\rm cuj}^{-1} < t_{\rm Hub}$, or $L_{\rm cuj} \gtrsim 10^{-2} T_{\rm hmr}^{-1}$.

The threshold $L_{\rm j} = 10^{-2.8}$ is adopted for two reasons. First, because the rate of appearance of new chaotic orbits slows down remarkably by increasing further $N_{\rm rp-max}$ (Kalapotharakos et al., 2004). Second, all the orbits with $L_{\rm cuj} > 10^{-2}$ have values of $L_{\rm j}$ well above the threshold $10^{-2.8}$, so they are certainly included in the set of chaotic orbits. This is seen in Figure 1, where all the detected chaotic orbits of the SC model are plotted on the $\log L_{\rm j} - \log L_{\rm cuj}$ plane.

Chaotic orbits in a 3D Hamiltonian system can be either fully chaotic, or partially chaotic. The fully chaotic orbits are characterized by two positive Lyapunov numbers, the first (or the maximal) LCN corresponding to $L_{\rm j}$ and a second LCN, smaller than $L_{\rm j}$. The partially chaotic orbits are characterized by only one positive LCN corresponding to $L_{\rm j}$ and they obey one more integral of motion beyond their binding energy. Due to this integral, partially chaotic orbits are confined in space, and are not allowed to diffuse to all directions.

In our distinction between ordered and chaotic orbits in terms of $L_{\rm j}$, partially and fully chaotic orbits are bunched together. Most of the chaotic orbits with large values of $L_{\rm j}$ are fully chaotic, e.g. orbits with $\log L_{\rm j} \gtrsim -2$ in Figure 1. Those with smaller values of $L_{\rm j}$ can be characterized as partially chaotic because their second Lyapunov number is either very small or zero. They obey an approximate integral of motion so they are confined to particular regions of phase space.

Muzzio and Mosquera (2004), Muzzio et al. (2005), in their study of the mass in chaotic motion in self-consistent models of stellar systems, have used a

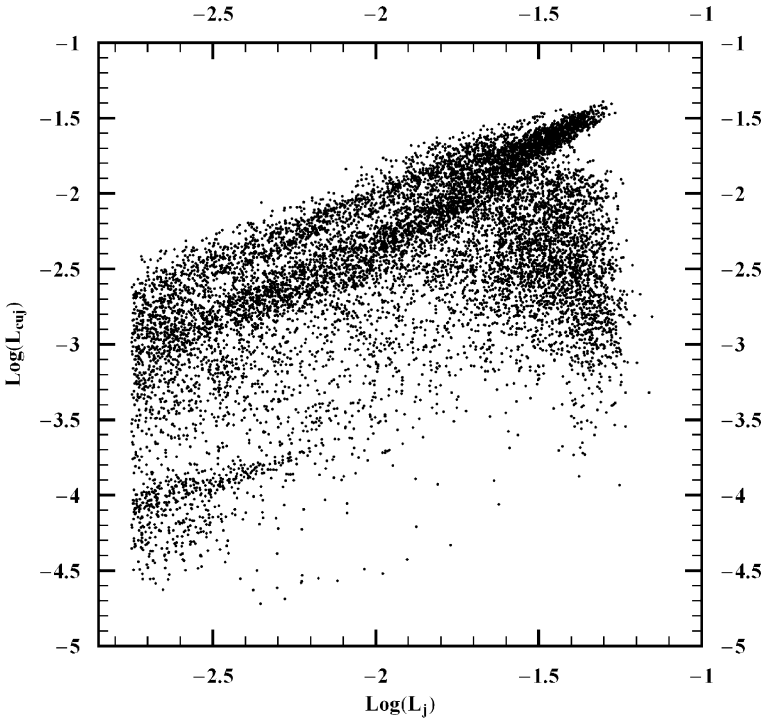


*Figure 1*. The chaotic orbits in the SC model detected by $L_{\rm j}$ above the threshold of $10^{-2.8}$ are plotted on the plane of log $L$j − log $L_{\rm cuj}$. Very small values of $L_{cuj}$ are only due to the orbits of long radial periods. The orbits with $\log L_{\rm cuj} > -2$ that can develop chaotic diffusion in a Hubble are well above the threshold of $\log L_{\rm j} = -2.8$. Partially chaotic orbits are found mainly among the orbits with low values of log $L_{\rm j}$.

common unit for the evaluation of the Lyapunov numbers (as in our $L_{\rm cuj}$). They evaluate both the first and the second FT-LCNs of the orbits above a threshold. They show that the orbits of their systems that are characterized as partially chaotic, but also those of the fully chaotic orbits with low values of the first FT-LCN, have different spatial distributions compared with the fully chaotic orbits with high values of the first FT-LCN. Fully chaotic orbits with low FT-LCN and partially chaotic orbits are confined in a prolate-triaxial distribution, while fully chaotic orbits with high FT-LCN show an almost spherical distribution. Fully chaotic orbits with low FT-LCN behave as partially chaotic for a long time. Therefore, a distinction between the chaotic orbits having a confined spatial distribution and those having an almost spherical distribution can be obtained by using the values of the first FT-LCN (small or large, respectively). It is not quite necessary to identify separately the partially and the fully chaotic orbits, although such a distinction can give more details about the spatial distribution of the orbits with low FT-LCN.

As it is well known, an alternative method to distinguish between ordered and chaotic motion is the frequency analysis method introduced by Laskar (1990). (See also Laskar et al., 1992; Laskar, 1993a, 1993b; Papaphillipou and Laskar, 1996, 1998). This method exploits the fact that the frequencies of ordered orbits remain constant in time (within the available accuracy). The frequencies of chaotic orbits, on the other hand, develop a considerable variability. The distinction is obtained by evaluating accurately the fundamental frequencies of the orbits.

For this purpose we use the FMFT code by Sidlichovsky and Nesvorny (1997) to find the fundamental frequencies $\nu_x$, $\nu_y$, $\nu_z$ of the oscillations of the orbits along the $x, y, z$ axes. Notice that these frequencies are measured in units of the inverse radial period of each particular orbit, as in the case of the $L_{\rm j}$.

In order to check the variability of the fundamental frequencies of the orbits in a particular snapshot of the potential (1), we select two spans for every orbit with the same number of radial periods $\Delta N_{\rm rp} = 300$, common for all the orbits. The run time of the orbit j is:

span(1): from $t = 0$ to $t = 300T_{\rm rj}$

span(2): from $t = 900T_{\rm rj}$ to $t = 1200T_{\rm rj}$.

The fundamental frequencies along the shortest axis $x$ (the most unstable direction in the system) are always larger and more sensitive than the fundamental frequencies along the other two axes. For this reason we use the quantity

$$\delta\omega_j = \frac{|\nu_{xj}^{(1)} - \nu_{xj}^{(2)}|}{\nu_{xj}^{(1)}} \tag{11}$$

as a measure of the variability of frequencies. The upper index gives the corresponding span from which the frequency is evaluated.

In terms of the three indices, $L_{\rm j}$, $AI_j$, $\delta\omega_{\rm j}$, we can obtain a very clear distinction between ordered and chaotic orbits. This can be seen in Figure 2a,b, where all the orbits of the two systems are plotted in the three-dimensional space $(\log AI_j, \log L_{\rm j}, \log \delta\omega_j)$. For most of the orbits ($\approx 95\%$) the index $\log AI_j$ works as a switch taking values either in the region from $-3$ to 0 for ordered orbits, or very small values, less than -10 for chaotic orbits. The intermediate values of $\log AI_j$ correspond to a relatively small number ($\approx 5\%$) of weakly chaotic orbits of the lane joining the two groups.

Using the above method we have found that in the SC model about 32% of the total mass moves in chaotic orbits and about 68% in ordered orbits. As we have checked, these fractions remain almost the same at various snapshots selected at very different times even larger than the Hubble time.

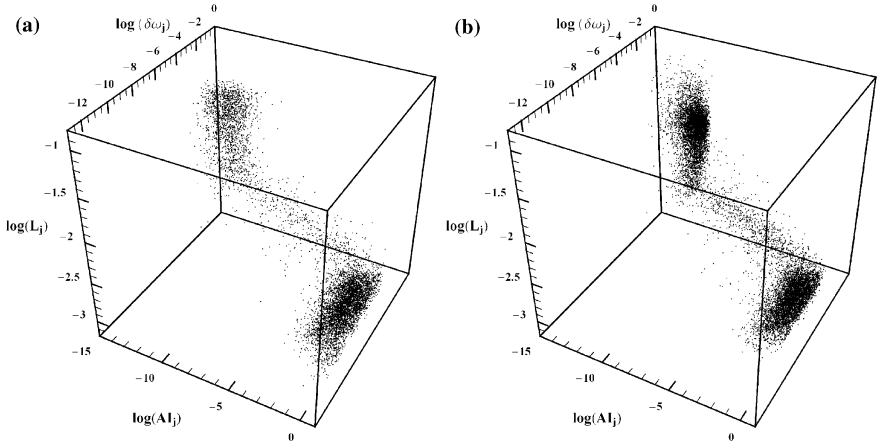


*Figure 2.* Distinction between ordered and chaotic orbits using the three indices $\log \mathrm{AI_j}, \log L_\mathrm{j}, \log \delta\omega_\mathrm{j}$ for the two models SC (a) and CM (b). The sensitivity of $\log AI_j$ is considerable larger than the sensitivity of the other two indices.

The identities of the particles in the groups are also well preserved, in spite of the noise due to the variations of the coefficients of the potential. Only a fraction of 1–2% of the total number of particles jump from one group to the other and vice versa.

It is worth noticing that Muzzio et al. (2005), in their smooth center model of an elliptical galaxy, have found a fraction of mass in chaotic motion of about 53%, i.e. considerably larger than in our study. Partially, this diffrence is due to an overestimation (with respect to our estimation) of chaos (especially in the low energy orbits) because of the use of a smaller threshold in their FT-LCN similar to $L_\mathrm{cuj}$. Another source of this difference is the fact that our SC model is more flat near the center than their model. However, their results are in agreement with our conclusion that, even in models of stellar systems with smooth centers, the fraction of mass in chaotic motion is not negligible. It is at least of the order of a few tens per cent, although in most of the chaotic orbits the corresponding Lyapunov numbers may be relatively small.

Applying our method to various snapshots of the CM model we find that at the snapshot of $t = 0$ the fraction of mass in chaotic motion is $\approx 80\%$. At the snapshot of $t = 150$ the chaotic mass is reduced to $\approx 58\%$, while at the snapshot of $t = 300$ this fraction falls down to $\approx 22\%$ and remains permanently (i.e. for a time much longer than a Hubble time) on this level, indicating that the system has reached a well established equilibrium. The reduction of the fraction of mass in chaotic motion from one snapshot to another is due to a process of self-organization occurring in the CM model that is discussed in Section 6.

## 4. The Frequency Map of the SC Model

We define the rotation numbers $v_y/v_x$ and $v_z/v_x$ and we mark the frequencies on the rotation number plane (e.g. as in Papaphillipou and Laskar, 1998; Wachlin and Ferraz-Mello, 1998; Valluri and Merritt, 1998; Holley-Bocklmann et al., 2002). Such diagrams are usually called frequency maps. Typical examples of orbits found in the SC model are shown in Figure 3a–f. The letters a,b,... label the rows of this figure. Every row gives the three projections of the same orbit on the planes $x-y, x-z, y-z$, respectively. Following a standard terminology (de Zeeuw, 1985; Statler, 1987), the types of ordered orbits found in this model can be classified in terms of their rotation numbers as follows:

(a) Box orbits. They are combinations of three oscillations along the $x, y, z$ axes. They can pass arbitrarily close to the center. Their rotation numbers $v_y/v_x$ and $v_z/v_x$ are irrational. The major axis of most of the box orbits is in average along the longest axis $z$ of the system but it performs two librational motions around the axis $z$ with constant irrational frequencies either on the $y-z$ or on the $x-z$ plane, filling in this way a region having the shape of a parallelepiped, with curved surfaces, (Figure 3a). This type of orbits is compatible only with triaxial equidensity surfaces.

(b) Inner Long Axis Tube (ILAT) orbits. Such orbits fill tube-like regions with maximum size along the longest axis $z$ (Figure 3b). The hole of the tube appears along the $z$ axis due to the component of the angular momentum of the orbit along this axis. For a number of ILAT orbits this hole may be small, so that they can pass quite close to the center. In this case the ILAT orbits resemble the box orbits. For this reason we call them box-like orbits. The ILAT orbits are characterized by the resonant value of the rotation number $v_y/v_x = 1$. Due to this resonance the major axis of the ILAT orbits describes a precession around the $z$ axis. This type of orbits is compatible with triaxial and prolate equidensity surfaces.

(c) Outer Long Axis Tube (OLAT) orbits. This is another type of resonant orbits with the same rotation number $v_y/v_x = 1$ as the ILAT orbits and with the hole of the tube being again along the longest axis $z$ (Figure 3c). The main difference of the OLAT from the ILAT orbits is that the major axis of the OLAT orbits oscillates up and down the $x-y$ plane instead of precessing around the $z$ axis. Furthermore, the angular momentum along the $z$ axis and the radius of the hole are larger compared with the corresponding quantities of the ILAT orbits. Thus, they do not approach so close to the center. This type of orbits is compatible with triaxial and prolate equidensity surfaces.

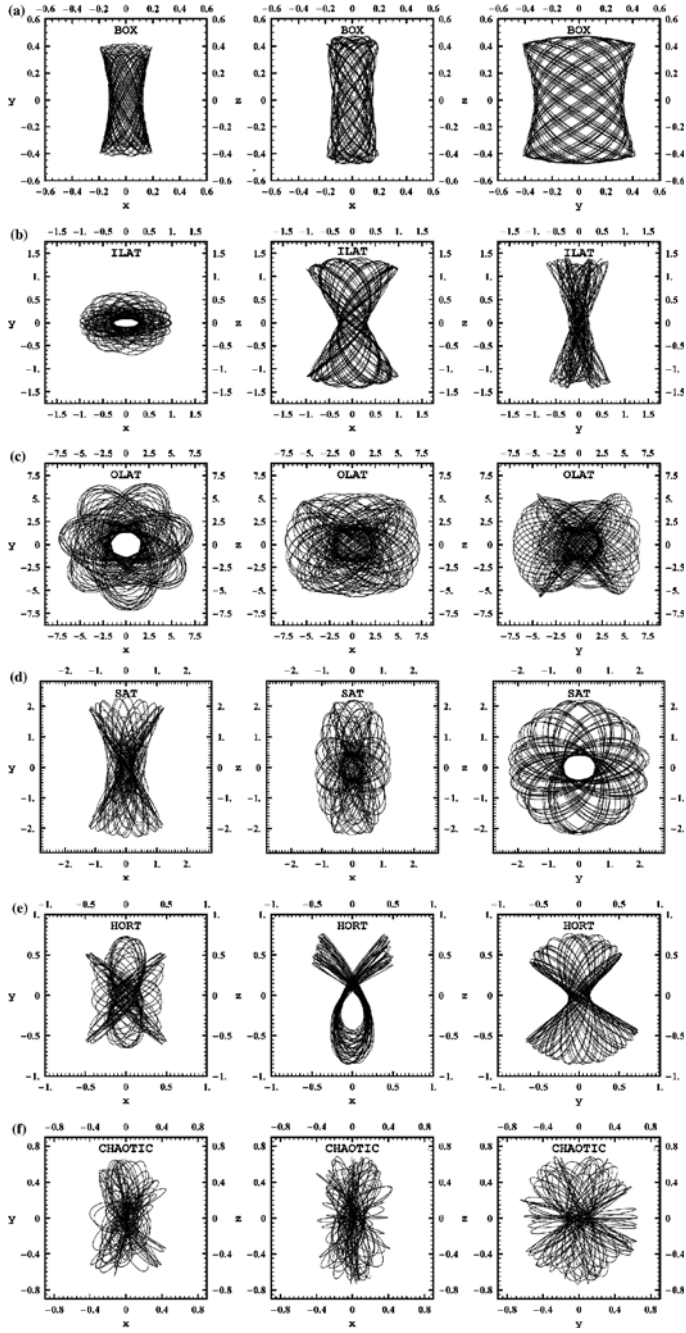


*Figure 3*. Examples of the various types of orbits of the particles in the SC model. Each row gives a type of orbit projected on the three planes $x$–$y$, $x$–$z$, $y$–$z$, respectively. The types of orbits are box (a), ILAT (b), OLAT (c), SAT (d), HORT (e), chaotic (f).

(d) *Short Axis Tube (SAT) orbits*. They form tubes surrounding the shortest axis $x$ (having their hole along this axis, Figure 3d). They are characterized by equal rotation numbers, i.e. $v_y/v_x = v_z/v_x$. Their major axis oscillates up and down the plane of the intermediate-longest axes ($y-z$ plane). Due to their angular momentum along the shortest axis they can not approach the center. They support the flatness of the system along the shortest axis. This type of orbits is compatible with triaxial and oblate equidensity surfaces.

(e) *Higher Order Resonant Tube (HORT) orbits*. These are tube-like ordered orbits corresponding to various resonances of higher order. For example the ratio of frequencies of the orbit in Figure 3e is approximately $v_z : v_x = 2 : 3$. In general, HORT orbits do no approach very near the center. This type of orbits is compatible only with triaxial equidensity surfaces.

(f) *Chaotic orbits* have been discussed in the previous section. Their rotation numbers vary irregularly in time. An example of chaotic orbit is shown in Figure 3f. This type of orbits is compatible with all the kinds of equidensity surface.

As it is well known the resonant orbits satisfy the condition of Diofantos

$$n_x v_x + n_y v_y + n_z v_z = 0, \tag{12}$$

where $n_x$, $n_y$ and $n_z$ are integers. If one of the three frequencies is irrational to the others the above equation is satisfied if the corresponding coefficient is zero. This is the case of the ILAT, OLAT and SAT orbits. For ILAT and OLAT orbits the vector $(n_x, n_y, n_z)$ that satisfies (12) is $(1, -1, 0)$, while for the SAT orbits this vector is $(0, 1, -1)$.

For the HORT orbit shown in Figure 3e $(n_x, n_y, n_z) = (-2, 0, 3)$. There are of course HORT orbits with non-zero integers in all the three components of the vector $(n_x, n_y, n_z)$ satisfying (12). For box orbits equation (12) is satisfied only for $(n_x, n_y, n_z) = (0, 0, 0)$.

As we will see by the end of this section a good number of the detected chaotic orbits follow the geometry of the above types of ordered orbits and they satisfy resonance conditions with a good accuracy for not negligible periods of time.

At high energy levels all the types of orbits are present but this is not the case at low energy levels. In order to study how the various types of orbits appear along different energy levels at a given snapshot of the potential, we run test particles scanning all the available phase space of the corresponding Hamiltonian at an energy level $h$. We find the fundamental frequencies of their orbits and construct the frequency map on the rotation number plane. This is repeated for a series of energy levels. The same process is repeated for the orbits of the real particles of the system with energies inside a small window (of width $\pm 1$) around $h$.

In Figure 4$a, \alpha, b, \beta, c, \gamma, d, \delta, e, \varepsilon, f, \zeta$ the rotation number planes of the orbits of test particles and the orbits of real particles are shown for comparison in pairs at energy levels

$$h = -80, -70, -60, -50, -40, -10,$$

respectively, as they result from the snapshot of the potential (1) at $t = 0$. The figures of the left column (labelled by Latin letters) give the orbits of test particles (covering all the available phase space at the corresponding energy). The figures of the right column (labelled by Greek letters) give the orbits of the real particles of the system (with energies inside a small window around the same value of energy).

We first describe Figure 4f ($h = -10$) where all the types of orbits are present as indicated in this figure.

The ILAT and OLAT orbits are located on two separated segments along a vertical line $v_y/v_x = 1$. The segment of ILAT is for $v_z/v_x \lesssim 0.7$. The almost empty part of this line near the value $v_z/v_x = 0.7$ corresponds to a zone of instability that separates these two families of orbits.

In Figure 4f the SAT orbits are located along the diagonal $v_y/v_x = v_z/v_x$. The box and the HORT orbits occupy a wide range on this plane with $v_z/v_x \lesssim 0.7$ and $v_y/v_x < 1$. The box orbits form an almost continuous distribution in this area, interrupted by straight lines corresponding to HORT orbits. The points that are irregularly dispersed in between the above types of orbits correspond to chaotic orbits.

As we can see in Figure 4$\zeta$ the real particles of the system at the same energy level occupy all the types of orbits of test particles and they are distributed in a rather similar way. However, this is not always the case especially for low energies as we will see below.

In the deepest parts of the potential only box and HORT orbits are allowed. For example, for $h = -80$ (Figure 4a) only box orbits appear (and a small number of HORT orbits that are not clearly seen in this figure). The same happens also for smaller energy levels. It is remarkable that on the rotation number plane the area of box orbits at low energy levels has a shape of a curvilinear triangle as in Figure 4a. The three corners of the triangle correspond to harmonic oscillations along the longest axis $z$ (top corner), the intermediate axis $y$ (left corner) and the shortest axis $x$ (right corner), with small amplitude of oscillations along the other axes in each case.

In Figure 4$\alpha$ the real particles of the system occupy preferably the left side of the triangle than the right side, which is almost empty. This is because of the self-consistency. The existence of stable orbits of test particles does not necessarily imply that these orbits can be occupied by real particles of the system. The orbits of real particles are further restricted by the self-consis-

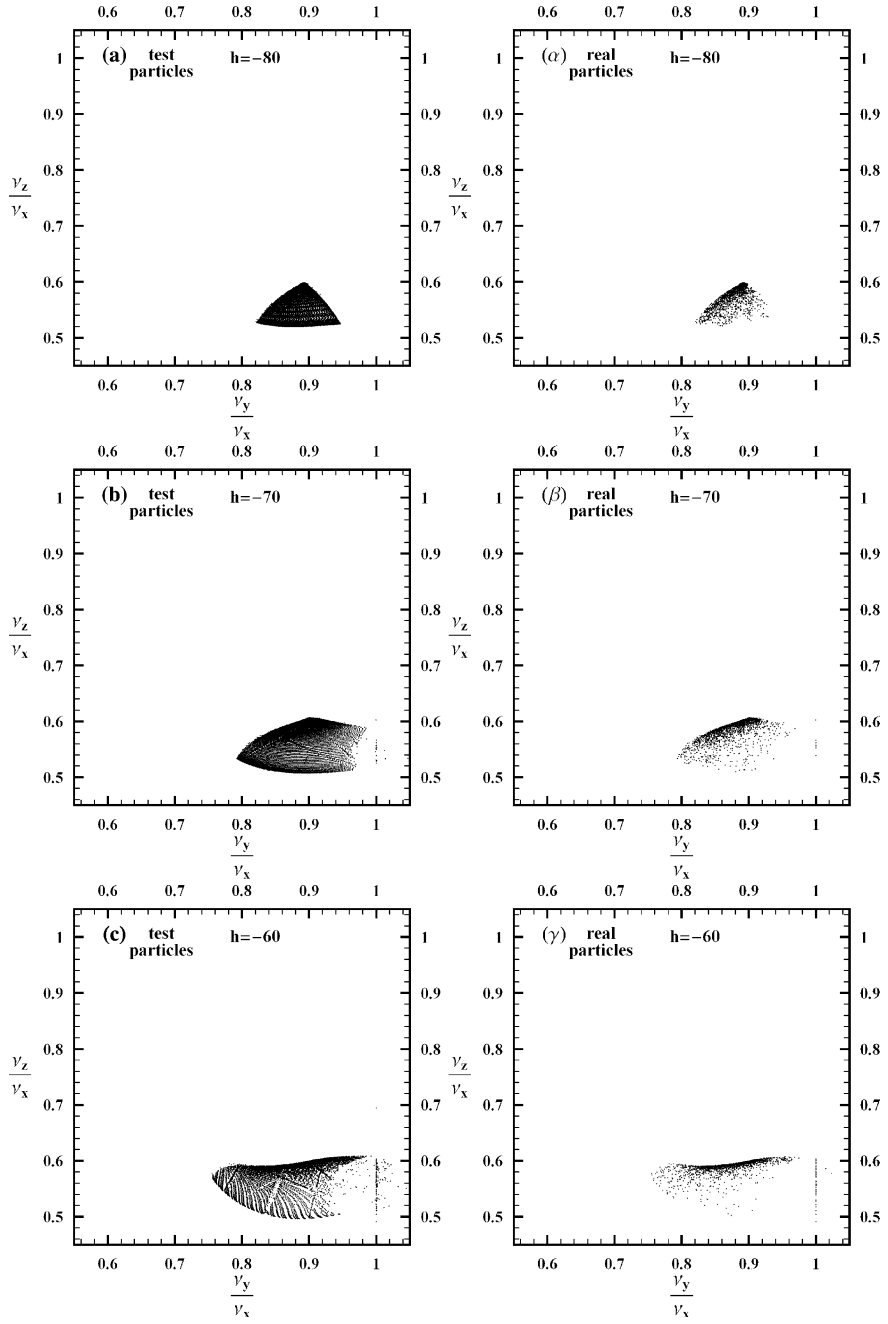


*Figure 4*. The rotation number plane at the energy levels $h = -80, -70, -60, -50, -40, -10$ for the snapshot at $t = 0$ of the potential (1) of the SC model. In the figures of the left column (a), (b), (c), (d), (e), (f) orbits of test particles are plotted scanning all the available phase space at every energy level. In the right column $\alpha$, $\beta$, $\gamma$, $\delta$, $\epsilon$, $\zeta$ the orbits of the real particles of the system with energies in a small window $\pm 1$ around the corresponding energy are plotted for comparison. The real particles of the system do not necessarily occupy all the available phase space, because they are further restricted by self-consistency.

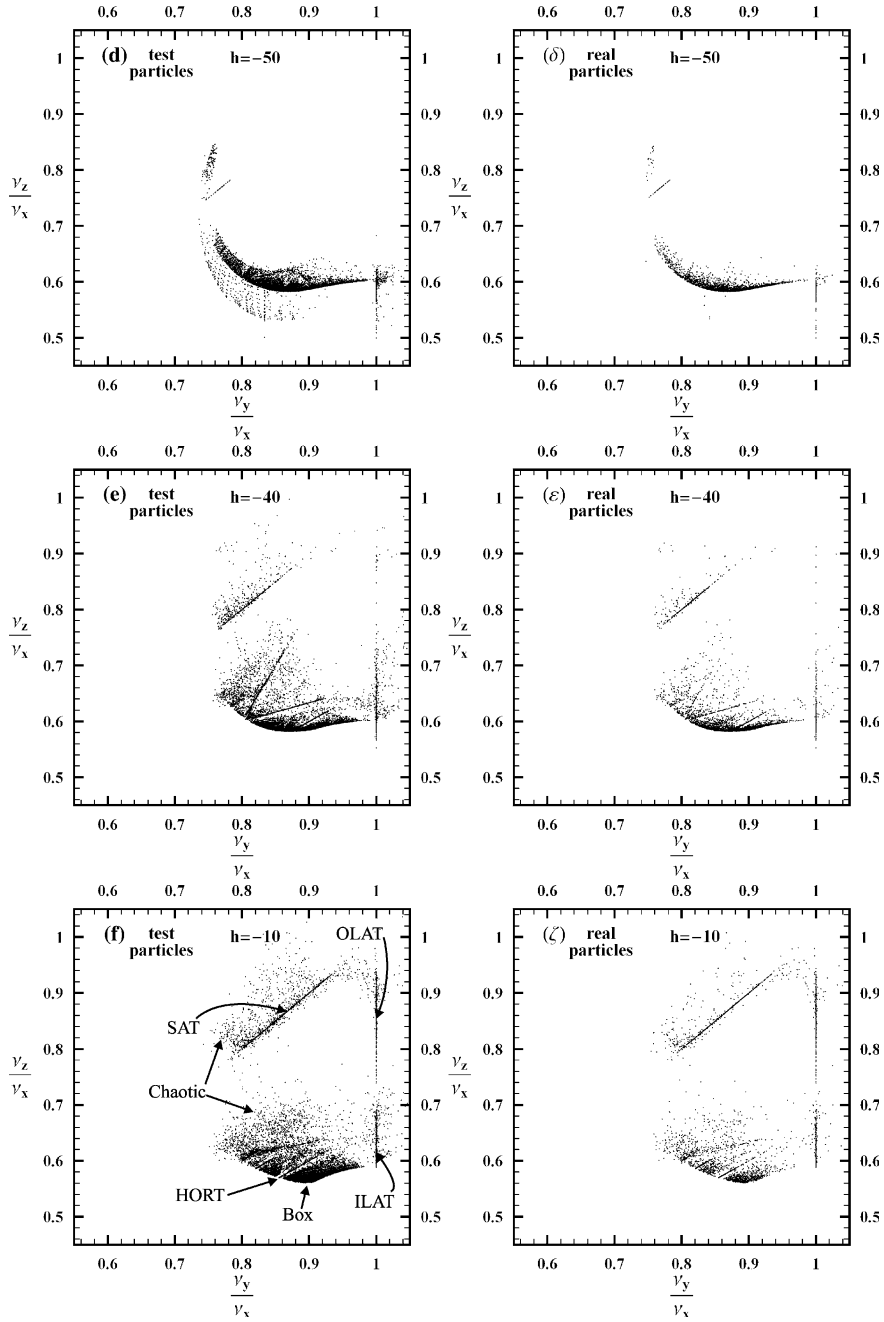


*Figure 4.* (Continued)

tency to follow a distribution that supports the equidensity surfaces having their axis along $y$ larger than their axis along $x$, otherwise the system could not be in equilibium.

In Figure 4b (for $h = -70$) the area of box orbits is expanded covering a wider range of values of $v_y/v_x$. The upper angle of the curvilinear triangle flattens. This flattening corresponds to the increase of the amplitude of the libration of the major axis of the box orbits either on the $y-z$ plane (expansion to the left), or on the $x-z$ plane (expansion to the right). The right corner of the triangle has been destroyed because the oscillation along the shortest axis has already been unstable. A weakly populated chaotic layer appears in this area separating the box orbits from the ILAT orbits, that start appearing at about this level of energy (a few points along the line $v_y/v_x = 1$). The left corner still exists, indicating that the corresponding oscillations (along the $y$ axis) are still stable. This corner is expanded to smaller values of $v_y/v_x$.

As shown in Figure 4$\beta$ the orbits of real particles again do not cover all the area of stable orbits of test particles. They are preferably located near the left-upper limit of this area because of self-consistency reasons, as explained above.

At the energy level $h = -60$ (Figure 4c) the area of box orbits is further expanded along smaller values of $v_y/v_x$, due to further increasing of the libration of the major axis on the $y-z$ plane. The area of box orbits takes the shape of a lane rather than a triangle. The upper limits of $v_z/v_x$ form a curved line with an inverse curvature than the previous curvature (from convex it becomes concave). This concavity becomes larger and larger as the energy increases. The box orbits of real particles lie preferably along this line (Figure 4$\gamma$).

For $h = -50$ (Figure 4d) the left end of the lane turns abruptly upwards. The box orbits at this end become unstable and the SAT orbits appear as a new family (short straight line with slope 1.0 in Figure 4d). As the energy increases the area of the SAT orbits increases. The orbits of real particles follow a roughly similar distribution (Figure 4$\delta$).

At the energy level of about $h = -40$ (Figure 4e,$\varepsilon$) the family of OLAT orbits appears (a few points along the line $v_y/v_x = 1$ with $v_z/v_x \gtrsim 0.75$. For higher energy levels all the types of orbits appear as in Figure 4f,$\zeta$.

As described in Section 3, we have found that the ordered and the chaotic components are respectively, $\approx 68\%$ and $\approx 32\%$ in the SC model. Furthermore, these fractions as well as the identities of particles in each type of motion are almost permanent.

All the ordered orbits (of all the energy levels) of the real particles in this system are plotted on the rotation number plane in Figure 5a, while the chaotic orbits are plotted in Figure 5b.

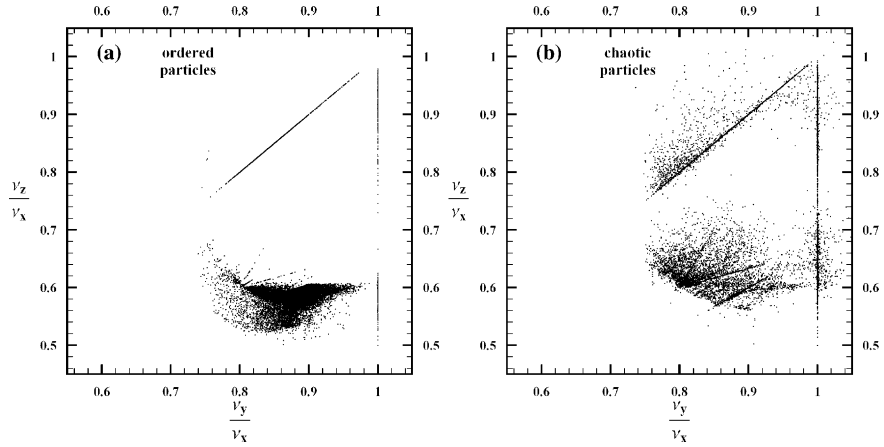


*Figure 5.* (a) All the ordered orbits of the SC model plotted on the rotation number plane independently of their energy. (b) As in (a) but for the chaotic orbits. A number of chaotic orbits are temporarily trapped near the resonant lines.

In Figure 5a we see clearly the groups of SAT, ILAT, OLAT and HORT orbits on sharp straight lines. The box orbits form a not very sharp area due to the superposition of the box orbits of different energy levels. Note that the majority of the ordered orbits, i.e. $\sim 91\%$ of the ordered component, moves in box (and HORT) orbits.

In Figure 5b we see that many chaotic orbits are located along resonant lines. These orbits diffuse mainly along the resonant lines. As long as they are trapped on a resonant line they maintain a very small or zero second FT-LCN, i.e. they are partially chaotic. We collect those of the chaotic orbits of Figure 5b that are projected upon the most important resonant lines and we plot them separately in Figure 6a. We plot also their distribution along the $\log L_j$ axis in Figure 6b by a dashed line together with the distribution of all the chaotic orbits (solid line). We see that among the more weakly chaotic orbits (i.e. $\log L_j \lesssim -2$) there is an almost constant difference between the values of the two curves at any given $L_j$. This means that there are many weakly or partially chaotic orbits located outside the resonant lines. These are mainly orbits resembling the box type. Among the more strongly chaotic orbits the ratio of the values of the dashed curve to the values of the solid curve decreases to zero as $\log L_j$ increases. The probability of more strongly chaotic orbits to be trapped along resonant lines is small.

As we have checked, due to the small variations of the potential, some of the resonant orbits can escape the resonant lines, but other chaotic orbits are trapped on the same resonant lines, so that the system preserves a dynamical equilibrium, in which the number of orbits in every type remains remarkably constant in time.

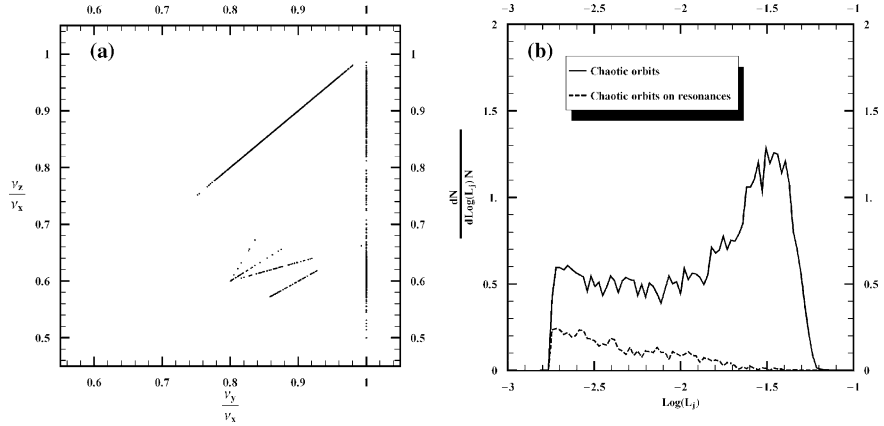


*Figure 6*. (a) A separate plot of those chaotic orbits in Figure 5b that occupy the most important resonant lines in the SC model. (b) Distribution of all the chaotic orbits (solid line) along the log $L_j$ axis and the distribution of the orbits in (a) (dashed line). For small values of $L_j$ there is a roughly constant difference between the two curves, due mainly to weakly chaotic orbits resembling box orbits. For large values of $L_j$ the relative occurrence of chaotic resonant orbits decreases considerably.

## 5. The Frequency Map of the CM Model

A similar analysis is performed in the CM model using the Hamiltonian (9) at a snapshot of the self-consistent potential corresponding to a run time $t = 150$ after the central mass is inserted.

At this snapshot, as mentioned in Section 3, we found that the fraction of mass in ordered motion ($L_j < 10^{-2.8}$) and in chaotic motion ($L_j > 10^{-2.8}$) are respectively, $\approx 42\%$ and $\approx 58\%$. All the particles of these two components, plotted on the rotation number plane, are shown in Figure 7a,b, respectively.

In Figure 7a we see that the particles of the ordered component belong to resonant orbits only, forming quite sharp straight lines. No box orbits appear at all. Also the ILAT type is almost absent. The majority ($\sim 95\%$) of the ordered orbits in this figure belong to SAT orbits, but there are some OLAT and HORT orbits as well.

On the other hand, the chaotic component, shown in Figure 7b, contains a large number of orbits in the area of box orbits. These orbits come from the box orbits in SC model that became chaotic by passing near the cental mass.

As in Figure 5b, the resonant lines in Figure 7b are occupied by a good number of weakly or partially chaotic orbits, diffusing mainly along the same resonant line. Due to the secular evolution of the potential these orbits escape from the resonant lines, but other chaotic orbits can be trapped along res-

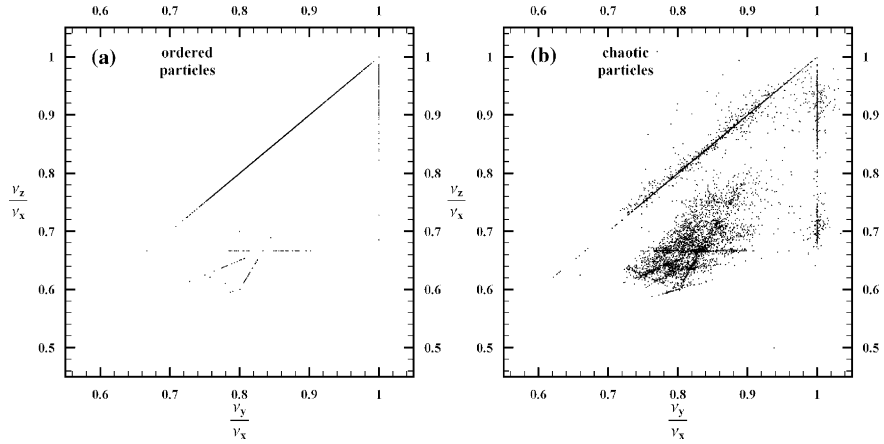


*Figure 7*. As in Figure 5a,b but for the CM model. Ordered motion (a) occurs in resonant orbits only. Orbits in the region of box and ILAT orbits are chaotic because of the central mass and they are shown in (b).

onant lines. As we will see in Section 6, trapping along the line ($v_z/v_y = 1$) of SAT orbits is much favored by the new shape of the potential, so most of the material is organized in SAT orbits.

In Figure 8a,b, which is similar to Figure 6a,b, but for the CM model, we see that almost all the weakly chaotic orbits ($\log L_j < -2$) are located on

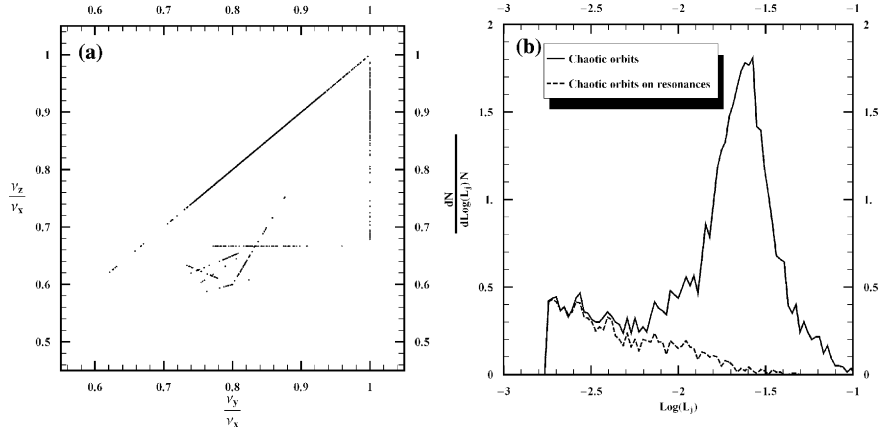


*Figure 8*. (a) A separate plot of those of the chaotic orbits in Figure 7b that occupy the most important resonant lines. (b) As in Figure 6b but for the CM model at $t = 150$. For small values of $L_j$ the difference between the two curves is quite small, unlike Figure 6b, because those of the weakly chaotic orbits that resemble box orbits (mentioned in Figure 6b) are converted either to more strongly chaotic orbits, or to resonant chaotic orbits. For large values of $L_j$ the relative occurrence of chaotic resonant orbits decreases considerably, as in Figure 6b.

resonant lines, unlike Figure 6b. This is because those of the weakly chaotic orbits in the SC model that were outside the resonant lines (resembling box orbits) have been converted partly to resonant orbits and partly to more strongly chaotic orbits in the CM model.

On the other hand, in Figure 8b, like in Figure 6b, more strongly chaotic orbits have a very small probability of being trapped along resonant lines.

An idea of how the various types of orbits are distributed at different energy levels at the snapshot $t = 150$ of the CM model is given in Figure 9a,$\alpha$,b,$\beta$. The left column (Figure 9a,b) refers to test particles, while the right column (Figure 9$\alpha$,$\beta$) refers to real particles.

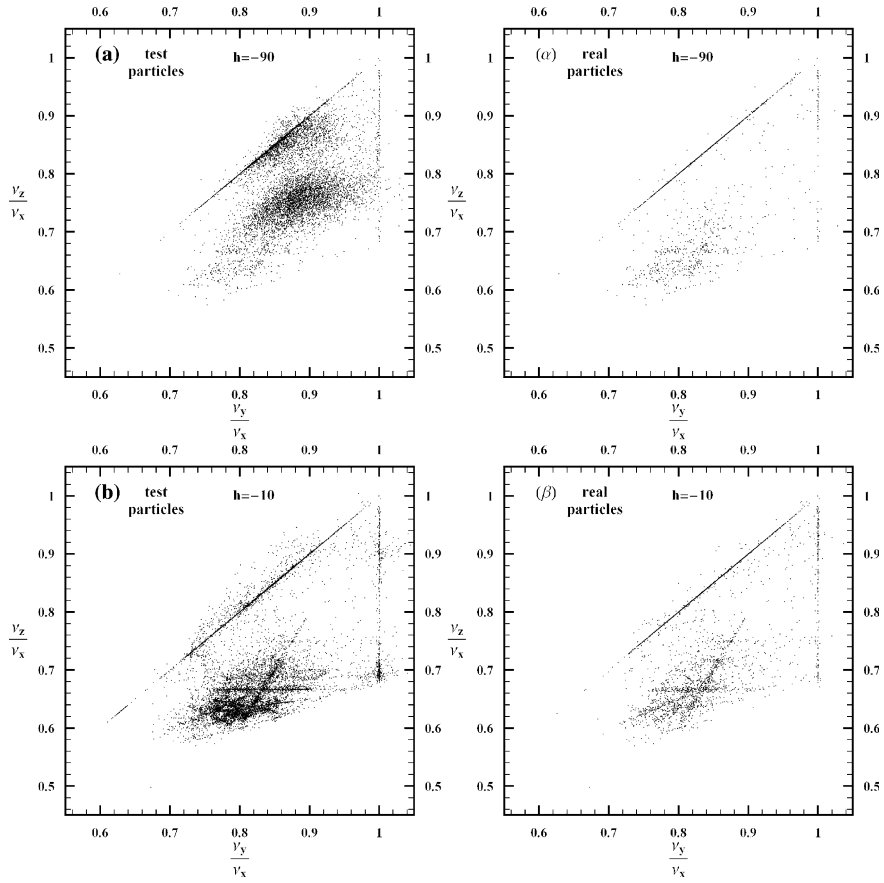


*Figure 9*. As in Figure 4, but for the snapshot at $t = 150$ of the CM model for two energy levels. (a),($\alpha$) are for the level $h = -90$. In this model SAT orbits appear from the lowest energy levels. In low energies the orbits of real particles do not follow the same distribution as the orbits of test particles. (b), ($\beta$) are for a high level $h = -10$. For high energies the distribution of real particles is not very different than the distribution of test particles.

At the level of $h = -90$ (Figure 9a,$\alpha$) the distribution of the orbits of real particles, outside the resonant lines, is not the same with the distribution of the orbits of test particles. Note that the system is not in equilibrium at this snapshot.

In these figures the majority of the orbits are chaotic, but there are also many ordered orbits mainly of SAT type. As we have seen (Section 4), in the SC model, at low energy levels, only ordered box (and a few HORT) orbits appear. At low energy levels ($h \lesssim -50$) of the SC model there are no SAT orbits at all. In contrast, in the CM model SAT orbits appear already from the lowest energy levels. This is another effect due to the presence of the central mass. The central mass favors ordered motion of particles in SAT orbits even at very low energy levels.

At higher energy levels of the CM model a relative increase of the ordered resonant orbits of all the types occurs. This can be seen on the rotation number plane as, for example, in Figure 9b,$\beta$ for $h = -10$.

## 6. Time Evolution and Self-organization of the CM Model

In this section we examine the evolutionary features of the CM model.

The introduction of the central mass destabilizes the well established initial equilibrium structure of the SC model. As we have seen above, almost all the box and the box-like (ILAT) orbits are converted into chaotic orbits. As a consequence, at the snapshot $t = 0$ of the CM model, the fraction of mass in chaotic motion is found to be about $\approx 80\%$, in contrast with the fraction $\approx 32\%$ of mass in chaotic motion found in the SC model. This serious increase of the mass in chaotic motion is accompanied by a serious change in the distribution of the Lyapunov numbers. This distribution shows a peak in the region of large values of $L_{\rm j}$, due mainly to box orbits that became chaotic.

As mentioned in Section 3, the diffusion of the orbit j is effective in a Hubble time, if $L_{\rm cuj} > 10^{-2}$. In the SC model, the mass in chaotic motion with $L_{\rm cuj} \gtrsim 10^{-2}$ is less than 8% and it is almost spherically distributed, unable to cause any considerable secular evolution in the system.

Notice that almost spherically distributed chaotic orbits cannot have serious consequences on producing secular evolution in the system by chaotic diffusion. Chaotic diffusion is important for producing secular evolution provided that the corresponding chaotic mass has initially an anisotropic spatial distribution. A more detailed examination of this effect is given in Voglis and Kalapotharakos (2005).

In the CM model, the mass in chaotic motion with $L_{\rm cuj} > 10^{-2}$ is $\approx 55\%$ at the snapshot $t = 0$ and it has an anisotropic distribution consistent with the configuration of the SC model. As this mass diffuses, it causes serious

changes on the equidensity surfaces and hence on the self-consistent equipotential surfaces of the system. Thus, the system becomes unstable and undergoes secular evolution towards an equilibrium state. During this evolution many chaotic orbits are trapped, by the new shapes of the equipotential surfaces, in different regions of the phase space, where they are converted to ordered orbits. The fraction of mass in ordered motion increases in time, while the mass in chaotic motion decreases. The system is self-organized. This process goes on until the remaining mass in chaotic motion cannot considerably affect the equipotential surfaces any more and the system achieves an equilibrium configuration.

The secular evolution of the CM model can be clearly demonstrated on the rotation number plane. We plot all the particles of the system on the rotation number plane using the Hamiltonian (9) for a series of successive snapshots of the potential taken from the self-consistent run. In this way we can follow the various types of orbits that are consistent with the corresponding snapshots of the potential.

As an example, four different snapshots are shown in Figure 10a–d at times $t = 10$, $t = 100$, $t = 200$, $t = 280$, respectively, where all the orbits of the real particles of the system are plotted. In these figures the areas of box, HORT and ILAT orbits are moving upwards approaching the line of the SAT orbits (compare Figure 10a–c). The number of all the other types of orbits decreases while the number of SAT orbits increases.

At the snapshot of $t = 280$ (Figure 10d) the majority of the orbits appear along the line of SAT orbits. There is also a smaller number of orbits along the line of OLAT orbits.Part of these orbits are expected to be (partially) chaotic with small values of their LCN. In any case a component of angular momentum along the shortest axis for the SAT orbits and along the longest axis for the OLAT orbits is approximately conserved.

The fraction of mass in chaotic motion at this snapshot ($t = 280$) is found $\approx 22\%$ and remains constant at this level. The system has achieved an almost oblate spheroidal equilibrium configuration supported by SAT orbits.

The time scale needed for the CM model to reach the equilibrium configuration is comparable with the Hubble time. It is remarkable that cuspy triaxial models with central mass of the same relative size, i.e. $m = 0.01$ investigated by other authors, (e.g. Holley-Bockelmann et al., 2002) appear considerably more stable compared with the CM model here. In Kalapotharakos et al. (2004), the CM model (called Q100) is compared with another model (called C100) containing a central mass of the same size. The C100 model evolves about six times more slowly than the Q100 model. The reason for this slow evolution is the fact that the C100 model contains initially (before the central mass is inserted) considerably less mass in box orbits and more mass in tube-like orbits. Stability in such models has a sensitive

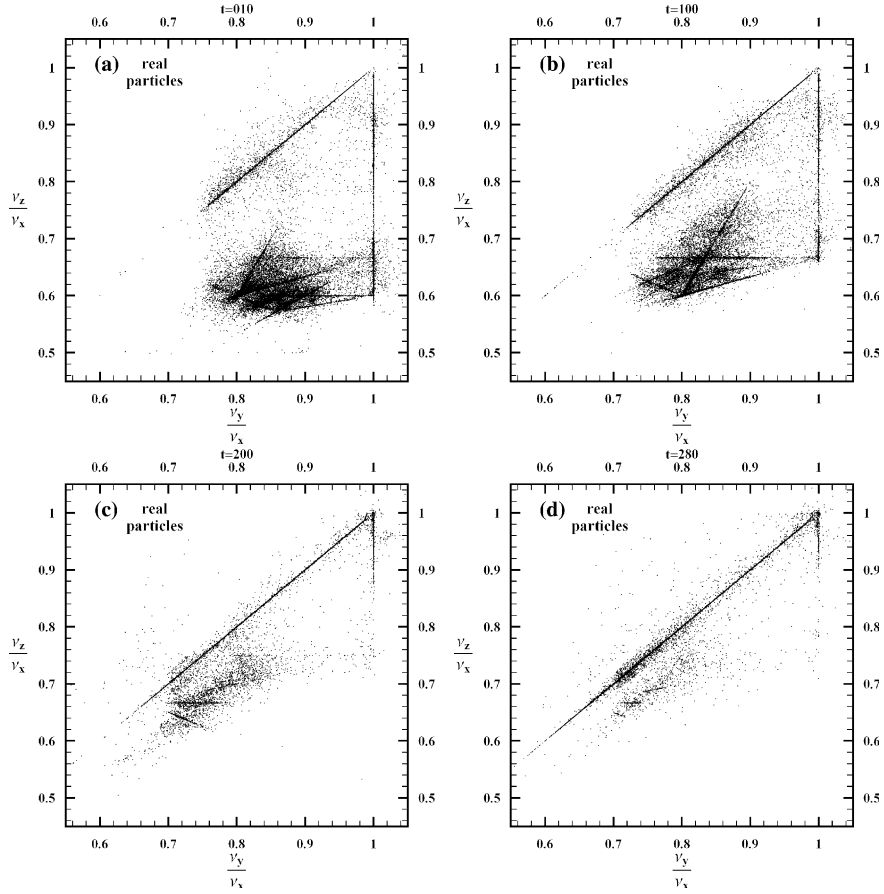


*Figure 10*. Four snapshots of the rotation number plane of the real particles of the CM model at times $t = 10$ (a), $t = 100$ (b), $t = 200$ (c), $t = 280$ (d), indicating the secular evolution of the system. Most of the chaotic orbits approach gradually the line of the SAT orbits and they are trapped on this line until an almost oblate spheroidal equilibrium configuration is achieved.

dependence on the number of box orbits supporting the triaxiality of the system. If triaxiality is mainly supported by combinations of tube orbits, rather than by box orbits, stable triaxial configurations are possible even with large central black holes.

The mechanism by which the chaotic orbits are converted to ordered orbits of the SAT type is discussed in detail in Kalapotharakos et al. (2004).

In brief, this mechanism is as follows: Due to the deflection of the box or box-like (ILAT) orbits as they pass near the center, the libration of their major axis around the $z$ axis becomes chaotic. Provided that the central mass is large enough the chaotic libration of the major axis, after a transient period, turns to rotation.

This rotation takes place preferably close to the $y-z$ plane, i.e. around the shortest axis ($x$-axis) of the system, because this orientation is more stable than others. Since the major axis of the orbit is no more trapped near the $z$-axis of the system, it can be directed along all the azimuthal angles on the $y-z$ plane. If this happens for a good number of orbits the predominance of the velocity dispersion along $z$ is lost and the two directions $y$ and $z$ tend to be equivalent as regards the dispersion of velocities. As a response the equidensity surfaces and the self-consistent equipotential surfaces approach an oblate spheroidal shape. Due to this change of the potential the chaotic orbits are gradually trapped and organized as SAT orbits. In their new SAT form these orbits do not approach the center any more.

The secular evolution ceases when the remaining chaotic orbits are isotropically distributed, or the rate of their passing near the central mass is too small to cause any considerable change on the system.

The secular evolution of the CM model can also be seen in terms of the triaxiality index $T$ defined as

$$T=\frac{c^2-b^2}{c^2-a^2}, \tag{13}$$

where a,b,c are the lengths of the principal axes of an equidensity surface with major axis $c=1$ in units of the half mass radius. The triaxiality index $T$ is equal to 0 for an oblate spheroidal surface and it is equal to 1 for a prolate spheroidal surface, while it is 0.5 for a maximally triaxial surface.

In Figure 11 the evolution of this index is plotted (in our two models for comparison) for times much longer than the Hubble time.

The SC model preserves the initial value of the triaxiality index $T\approx 0.9$, indicating that this model preserves its initial triaxial shape (close to a prolate shape) during all this time.

On the contrary, the triaxiality index of the CM model, starting from the same initial value, decreases tending to a small constant value. This decrease is irreversible. The index $T$ remains permanently close to zero, indicating that the system has achieved an almost oblate spheroidal equilibrium configuration. In this configuration the majority of orbits are of the SAT type as we have seen above (Figure 10c).

## 7. Summary and Conclusions

In terms of the fundamental frequency analysis we have investigated all the types of orbits that are described by the particles in the two examined N-body systems, i.e. a SC and a model with a large CM.

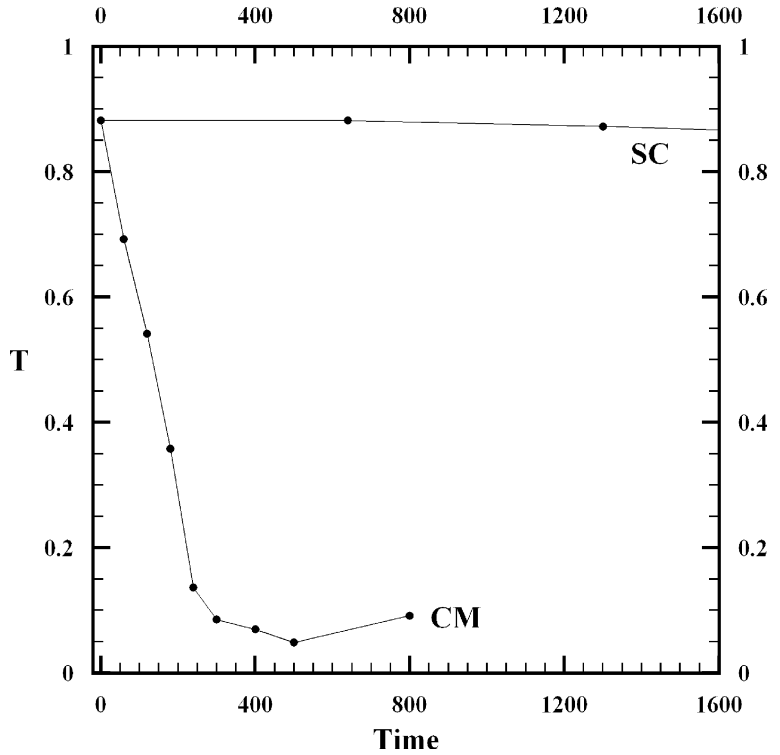


*Figure 11.* The secular evolution of the CM model in comparison with the stability of the SC model for times much longer than a Hubble time expressed in terms of the triaxiality index T. In the SC model T remains remarkably constant at the initial value $T \approx 0.9$ for long time. In the CM model T starts from this value and decreases approaching the zero value in a time scale of about one Hubble time when an almost oblate spheroidal equilibrium configuration is established.

The investigation combines the results of the fundamental frequency analysis with the results obtained by distinguishing chaotic from ordered orbits in terms of $L_j$, i.e. the Specific Finite Time Lyapunov Characteristic Number (S-FT-LCN) and the Alignment Index $AI_j$, a method introduced in a previous paper. The use of $L_j$ has several pros and cons with respect to the use of $L_{cuj}$, i.e. the Finite Time Lyapunov Characteristic Number in common units (CU-FT-LCN), that are discussed in Section 3. We show that the alignment index can make a considerably sharper distinction than the distinction obtained by the variability of frequencies $\delta\omega_j$ or by the rate of logarithmic divergence $L_j$ of the orbits (Figure 2).

We find that the SC model is stable. It contains a large fraction of ordered orbits ($\approx 68\%$ of the total mass). The main part of them are box orbits, but there are also many resonant tube orbits of various types, i.e. ILAT, OLAT,

SAT and HORT. On the rotation number plane these types of orbits occupy different loci, so they can be easily recognized, e.g. all the tube orbits are plotted along their characteristic resonant lines. At low energy levels only box and HORT orbits are present. As the energy increases the other types of tube orbits appear in the sequence ILAT, SAT, OLAT.

Among the chaotic orbits in this model, many of them are weakly or partially chaotic. Part of them resemble box orbits, but another part is trapped along resonant lines. More strongly chaotic orbits have small probability of being trapped along resonant lines.

In spite of the noise of the potential in a self-consistent run of the SC model, the number of particles occupying the various types of orbits is remarkably constant. This is obtained by a dynamical equilibrium established between the orbits that escape from a resonant line and the orbits that are trapped in this resonant line.

Comparing the distribution of the orbits of the real particles on the rotation number plane with the orbits of test particles, we conclude that extensive stable regions of phase space remain empty, i.e. they are not occupied by real particles of the system. This effect is due to the self-consistency of the system. Self-consistent equilibrium imposes serious limitations on the distribution of the real particles. These limitations are more severe than the limitations imposed by the stability of the orbits. Thus, finding stable orbits in a given galactic potential does not guarantee the existence of mass there and finding unstable regions does not guarantee the lack of mass there. This remark underlines the significance of the self-consistent models in studying galactic structures.

The empty stable regions are more pronounced in the low energy orbits, where chaos is weak and the chaotic orbits are rare. As the binding energies increase the orbits of real particles are in a better agreement with the orbits of test particles. In high binding energies real particles tend to occupy most the available phase space, either by ordered or by chaotic orbits.

The CM model is initially unstable. It presents a secular evolution due to the large amount of mass in chaotic motion produced by the central mass. This is initially about 80%. Most of this mass (about 55%) is characterized by Lyapunov times $L_{\mathrm{cuj}}^{-1} < 100 T_{\mathrm{hmr}}$, i.e. less than one Hubble time, and it has initially an anisotropic spatial distribution forming the bar of the system. Due to the diffusion of these orbits, the initially bar-like equipotential surfaces are gradually deformed approaching oblate spheroidal shapes with their flatness along the $x$ axis. As we have seen, by representing the orbits on the rotation number plane at various successive snapshots, during this deformation of the system, chaotic orbits are gradually converted to ordered orbits mainly of SAT type.

The secular evolution of the CM model ceases and equilibrium is established, when the remaining number of chaotic orbits is no more efficient to cause any considerable changes on the system, either because it is isotropically distributed, or because the rate of orbits that pass near the center is small.

The oblate spheroidal equilibrium configuration, established by the end of the secular evolution, is supported mainly by SAT orbits preserving the component of their angular momentum along the shortest axis. The orbital structure of this system is remarkably simpler than the orbital structure of a triaxial configuration.

## Acknowledgements

We wish to thank Drs Allen, Palmer and Papaloizou as well as Sidlichovsky and Nesvorny for their codes. We also wish to thank the referee for his comments that helped to improve the presentation of the paper and prof. G. Contopoulos for useful discussions. This work is supported by a research program of the EMPEIRIKEION Foundation. C.K. wishes to thank the Greek State Scholarship Foundation (I.K.Y) for financial support.

## References

Allen, A. J., Palmer, P. L. and Papaloizou, J.: 1990, 'A conservative numerical technique for collisionless dynamical systems – Comparison of the radial and circular orbit instabilities', *MNRAS* **242**, 576–594.

Contopoulos, G., Voglis, N., Kalapotharakos, C.: 2002, 'Order and chaos in self-consistent galactic models', *Celest. Mech. Dynam. Astron.* **83**, 191–204.

Cretton, N. and van den Bosch, F. C.: 1999, 'Evidence for a massive black hole in the S0 galaxy NGC 4342', *Astrophys. J.* **514**, 704–724.

de Zeeuw, T.: 1985, 'Elliptical galaxies with separable potentials', *MNRAS* **216**, 273–334.

Faber, S. M., Tremaine, S., Ajhar, E. A., Byun, Y., Dressler, A., Gebhardt, K., Grillmair, C., Kormendy, J., Lauer, T. R. and Richstone, D.: 1997, 'The centers of early-type galaxies with HST. IV. central parameter relations', *Astron. J.* **114**, 1771–1796.

Ferrarese, L., van den Bosch, F. C., Ford, H. C., Jaffe, W. and O'Connell, R. W.: 1994, 'Hubble space telescope photometry of the central regions of Virgo cluster elliptical galaxies. 3: Brightness profiles' *Astron. J.* **108**, 1598–1609.

Fridman, T. and Merritt, D.: 1997, 'Periodic orbits in triaxial galaxies with weak cusps' *Astron. J.* **114**, 1479–1487.

Gebhardt, K., Richstone, D., Ajhar, E. A., Lauer, T. R., Byun, Y., Kormendy, J., Dressler, A., Faber, S. M., Grillmair, C. and Tremaine, S.: 1996, 'The centers of early-type galaxies with HST. III. non-parametric recovery of stellar luminosity distribution', *Astron. J.* **112**, 105–113.

Gebhardt, K., Richstone, D., Kormendy, J., Lauer, T. R., Ajhar, E. A., Bender, R., Dressler, A., Faber, S. M., Grillmair, C., Magorrian, J. and Tremaine, S.: 2000, 'Axisymmetric, three-integral models of galaxies: A massive black hole in NGC 3379', *Astron. J.* **119**, 1157–1171.

Gerhard, O. E. and Binney, J.: 1985, 'Triaxial galaxies containing massive black holes or central density cusps', *MNRAS* **216**, 467–502.

Holley-Bockelmann, K., Mihos, J. C., Sigurdsson, S. and Hernquist, L.: 2001, 'Models of cuspy triaxial galaxies', *Astrophys. J.* **549**, 862–870.

Holley-Bockelmann, K., Mihos, J. C., Sigurdsson, S. Hernquist, L., Norman, C.: 2002, 'The evolution of cuspy triaxial galaxies harboring central black holes', *Astrophys. J.* **567**, 817–827.

Kalapotharakos, C., Voglis, N. and Contopoulos, G.: 2004, 'Chaos and secular evolution of triaxial N-body galactic models due to an imposed central mass', *Astron. & Astrophys.* **428**, 905–923.

Kandrup, H. E. and Sideris, I. V.: 2002, 'Chaos in cuspy triaxial galaxies with a supermassive black hole: A simple toy model', *Celest. Mech. Dynam. Astron.* **82**, 61–81.

Kandrup, H. E. and Siopis, Ch.: 2003, 'Chaos and chaotic phase mixing in cuspy triaxial potentials', *MNRAS* **345**, 727–742.

Kormendy, J. and Richstone, D.: 1995, 'Inward bound – the search for supermassive black holes in galactic nuclei', *Ann. Rev. Astron. Astrophys.* **33**, 581–624.

Kormendy, J., Bender, R., Magorrian, J., Tremaine, S., Gebhardt, K., Richstone, D., Dressler, A., Faber, S. M., Grillmair, C. and Lauer, T. R.: 1997, *Astrophys. J. Letters* **482**, 139–144.

Kormendy, J., Bender, R., Evans, A. S. and Richstone, D.: 1998, 'The mass distribution in the elliptical galaxy NGC 3377: Evidence for a $2 \times 10^8 M_\odot$ black hole', *Astron. J.* **115**, 1823–1839.

Laskar, J.: 1990, 'The chaotic motion of the solar system – A numerical estimate of the size of the chaotic zones', *Icarus* **88**, 266–291.

Laskar, J.: 1993a, 'Frequency analysis of a dynamical system', *Celest. Mech. Dynam Astron.* **56**, 191–196.

Laskar, J.: 1993b, 'Frequency analysis for multi-dimensional systems. Global dynamics and diffusion', *Physica D* **67**, 257–281.

Laskar, J., Froeschle, C. and Celletti, A.: 1992, 'The measure of chaos by the numerical analysis of the fundamental frequencies. Application to the standard mapping', *Physica D* **56**, 253–269.

Lauer, T. R., Ajhar, E. A., Byun, Y. I., Dressler, A., Faber, S. M., Grillmair, C., Kormendy, J., Richstone, D. and Tremaine, S.: 1995, 'The Centers of Early-Type Galaxies with HST.I.An Observational Survey', *Astron. J.* **110**, 2622–2654.

Lichtenberg, A. J. and Lieberman, M. A.: 1992, Regular and Chaotic Dynamics', Springer-Verlag, New York..

Magorrian, J., Tremaine, S., Richstone, D., Bender, R., Bower, G., Dressler, A., Faber, S. M., Gebhardt, K., Green, R., Grillmair, C., Kormendy, J. and Lauer, T.: 1998, 'The demography of massive dark objects in galaxy centers', *Astron. J.* **115**, 2285–2305.

Merritt, D. and Ferrarese, L.: 2001, 'Black hole demographics from the $M_\bullet - \sigma$ relation', *MNRAS* **320**, 30–34.

Merritt, D. and Fridman, T.: 1996, 'Triaxial galaxies with cusps', *Astrophys. J.* **460**, 136–162.

Merritt, D. and Quinlan D. G.: 1998, 'Dynamical evolution of elliptical galaxies with central singularities', *Astrophys. J.* **498**, 625–639.

Merritt, D. and Valluri, M.: 1996, 'Chaos and mixing in triaxial stellar systems', *Astrophys. J.* **471**, 82–105.

Muzzio, J. C. and Mosquera, D. E.: 2004, 'Spatial structure of regular and chaotic orbits in self-consistent models of galactic satellites' *Celest. Mech. Dynam. Astron.* **88**, 379–396.

Muzzio, J. C., Carpintero, D. D. and Wachlin, F. C.: 2005, 'Spatial structure of regular and chaotic orbits in a self-consistent triaxial stellar system' *Celest. Mech. Dynam. Astron.* **91**, 173–190.

Papaphilippou, Y. and Laskar, J.: 1996, 'Frequency map analysis and global dynamics in a galactic potential with two degrees of freedom', *Astron. & Astrophys.* **307**, 427–449.

Papaphilippou, Y. and Laskar, J.: 1998, 'Global dynamics of triaxial galactic models through frequency map analysis', *Astron. & Astrophys.* **329**, 451–481.

Poon, M. Y. and Merritt, D.: 2002, 'Triaxial black hole nuclei', *Astrophys. J.* **568**, 89–92.

Poon, M. Y. and Merritt, D.: 2004, 'A self-consistent study of triaxial black hole nuclei', *Astrophys. J.* **606**, 774–787.

Siopis, Ch.: 1999, PhD thesis, University of Florida.

Siopis, Ch. and Kandrup, H. E.: 2000, 'Phase-space transport in cuspy triaxial potentials: Can they be used to construct self-consistent equilibria?', *MNRAS* **319**, 43–62.

Sidlichovsky, M. and Nesvorny, D.: 1997, 'Frequency modified Fourier transform and its applications to asteroids', *Celest. Mech.* **65**, 137–148.

Skokos Ch.: 2001, 'Alignment indices: A new, simple method for determining the ordered or chaotic nature of orbits', *J. Phys. A* **34**, 10029–10043.

Statler, T. S.: 1987, 'Self-consistent models of perfect triaxial galaxies', *Astrophys. J.* **321**, 113-152.

Valluri, M. and Merritt, D.: 1998, 'Regular and chaotic dynamics of triaxial stellar systems', *Astrophys. J.* **506**, 686–711.

van der Marel, R. P., de Zeeuw, P. T. and Rix, H. W.: 1997, 'Improved evidence for a black hole in M32 from HST/FOS spectra. I. Observations', *Astrophys. J.* **488**, 119–135.

van der Marel, R. P., and van den Bosch F. C.: 1998, 'Evidence for a $3 \times 10^8 M_{\odot}$ black hole in NGC 7052 from hubble space telescope observations of the nuclear gas disk', *Astron. J.* **116**, 2220-2236.

Voglis, N., Kalapotharakos, C.: 2005, 'The role of ordered and chaotic motion in N-body models of elliptical galaxies', in A. M. Fridmann, M. Ya Marov and I. G. Kovalenko (eds.), *Progress in the Study of Astrophysical Disks: Collective and Stochastic Processes and Computation Tools*, ASSL series, 2005, Kluwer Academic Press (in press).

Voglis, N., Contopoulos, G. and Efthymiopoulos, C.: 1998, 'Method for distinguishing between ordered and chaotic orbits in four-dimensional maps', *Phy. Rev. E* **57**, 372–377.

Voglis, N., Contopoulos and G., Efthymiopoulos, C.: 1999, 'Detection of ordered and chaotic motion using the dynamical spectra', *Celest. Mech. Dynam. Astron.* **73**, 211–220.

Voglis, N., Kalapotharakos, C. and Stavropoulos, I.: 2002, 'Mass components in ordered and in chaotic motion in galactic N-body models', *MNRAS* **337**, 619–630.

Wachlin, F. C. and Ferraz-Mello, S.: 1998, 'Frequency map analysis of the orbital structure in elliptical galaxies', *MNRAS* **298**, 22–32.